Restoration of Radiographic Neutron Image Using Single-Channel Blind Deconvolution

Y. Khairiah[1,2,*], A. Mohd Zaid[1], and I. Haidi[1]
[1] School of Electrical and Electronic Engineering, Universiti Sains Malaysia, Nibong Tebal, Penang, Malaysia
[2] Reactor Technology Center, Malaysian Nuclear Agency, Bangi, Malaysia
Email: khairiah@nm.gov.my (Y.K.), mza@usm.my (A.M.Z.), haidi@usm.my (I.H.)

***Abstract*—This paper addresses the challenge of accurately estimating the 2D Point Spread Function (PSF) or blur kernel in neutron radiography, where traditional methods, such as the Edge Spread Function (ESF), prove time-consuming and reliant on manual edge selection. The proposed alternative introduces a robust sparse image prior known as the enhanced Patch-Wise Intensity (EPI) image prior in a single-channel blind deconvolution algorithm, avoiding the need for intricate devices like pinhole or slit phantoms. Leveraging regularization and optimization techniques, the algorithm efficiently estimates PSF in a single image through a multi-layer iterative alternating approach. The study aims to enhance PSF accuracy, leading to a more accurate solution to the neutron image restoration problem. Comparative results with real neutron images indicate the proposed method outperforms ESF, demonstrating improved overall image quality both visually and quantitatively in terms of blind/no reference evaluation (BRISQUE).**

***Index Terms*—Point Spread Function (PSF) estimation, blind deconvolution, neutron images and image restoration**

I. Introduction

Neutron Radiography (NR), a non-destructive imaging technique that utilizes neutron radiation to probe the internal structure of objects, is technically similar to X-ray radiography. This imaging technique excels in materials characterization, defect detection, and analysis of various opaque objects particularly useful for imaging materials that are difficult to penetrate with X-rays, such as metals or materials with high atomic numbers. Neutrons have high penetration capabilities into all types of materials, including heavy metals, and are sensitive to many light elements, especially hydrogen [1–3]

Although powerful and unique, neutron images from low-power research reactors are usually degraded. Even though there are several factors responsible for this degradation, the problem is mainly due to the beam collimation ratio which is not sufficiently large in order to make a parallel beam a valid assumption for NR projection.

The study to improve the quality of the degraded neutron images has high research value and practical significance for analyzing and detecting the observed object's inner structures and features. The basic principle of a neutron radiography facility is a pinhole camera. In a pinhole concept, the tiny aperture makes the sharpest image, while a big hole produces a blurry image.

Blurring associated with a lack of collimation in the beam gives rise to blurring in neutron images. A collimator in a neutron radiography plays a crucial role in controlling, shaping, and focusing the neutron beam to achieve high-quality images. The beam collimation L/D ratio in neutron radiography facility is illustrated in Fig. 1, where L is the length between the smallest diameter of the collimator and the sample and D is the smallest diameter of the collimator. This L/D ratio defines the geometrical blurring of the neutron imaging facility. In general, the L/D ratio of state-of-the-art neutron radiography facilities generally lies in the range of 100 to 500 [4].

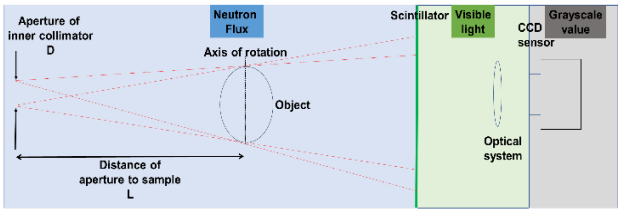

Fig. 1. The definition of beam collimation, (L/D) ratio in a typical NR image capturing system.

In contrast to the X-ray imaging system, the source of neutron radiography is not a point source but an extended aperture. The finite size D of the aperture is the main reason for geometrical blurring. The main reason for using this extended aperture in a low-power reactor is to guarantee that enough flux reaches the sample position. Increasing the L/D ratio in most facilities is not a viable option due to the necessity of facility reconstruction.

However, the L/D ratio is the main, but not the only, challenge connected with blurring in neutron radiography. The scintillator-based digital detectors used in neutron radiography also have limitations in terms of spatial resolution and sensitivity. This can result in blurry images and difficulties in distinguishing fine details or small defects. Hence, the imaging detector and large-aperture neutron source are the main contributors to the blurring of the neutron images.

Following the basic mathematical fundamentals of the degradation theory, the image blurring can be modeled as a convolution operation, given by

$$B = (k * L) + N \quad (1)$$

Manuscript received September 1, 2023; revised November 19, 2023; accepted January 18, 2024.
*Corresponding author

where B represents the blurred image, L refers to an unknown latent or sharp image, and k is the blur kernel or point spread function (PSF). The additive noise process N may originate during image acquisition or transmission. The symbol "*" represents the two-dimensional convolution operator.

Image deblurring is a process of the inverse of the convolution, or, in short, deconvolution. Referring to Eq. (1), with a known k, the image deblurring is the process of deconvolution. The quality of the image deconvolution depends on the accuracy of the PSF estimation method. There are two major classes in image deblurring: (1) non-blind deconvolution method has a prior known k; (2) blind deconvolution deblurring refers to the problem of recovering the sharp image without exact knowledge of k.

Blind deconvolution, an ill-posed inverse problem, is a very challenging task in image processing, and it has numerous applications. In general, the PSF needs to be measured to remove the blurring. The PSF can be described by a mathematical model that can be constructed from a function rather than through experimentation. Blind deconvolution attempts to iteratively solve for both the PSF and the sharp image from a blurry image by incorporating general knowledge of both the PSF and sharp image into a cost function in a standard model. Hence, the blind deblurring is complicated and much more challenging than the sharp image, and PSF estimation must be performed simultaneously.

Many research studies have been devoted to blind deconvolution. There are two major trends in blind image deblurring: optimization-based and learning-based. The optimization-based models are explicitly defined, and the prior knowledge is carefully included in the solution. In contrast to optimization-based models, learning-based models do not take advantage of prior knowledge and instead use large datasets to predict an unknown solution to the inverse problem. However, the success of learning-based models heavily depends on the consistency between the training data and the test data. Due to the lack of neutron image datasets, we focus on an optimization-based approach for neutron image deblurring.

Generally, sharp edges are preferred in PSF estimation. However, identifying a suitable, significant sharp edge feature within a blurred image is crucial to this method. A key criterion is that the selected edge should exhibit homogeneity on both of its sides. Subsequently, the process entails extracting the intensity line profile of the identified edge.

The neutron community commonly utilizes the Edge Spread Function (ESF) for PSF estimation. This method is a non-iterative edge-profile method to estimate the PSF. This method involves selecting a sharp edge or boundary in a known object. Researchers take the first derivative of the ESF and then employ a functional fitting procedure to estimate the Line Spread Function (LSF), or the estimation of the PSF. It is very common practice in this method to assume that the PSF is symmetrical, meaning that its 1D patterns in the horizontal and vertical directions are similar. The standard deviation of the LSF corresponds to the standard deviation of the symmetric two-dimensional PSF. Once the PSF is estimated, the classical Richardson-Lucy non-blind deconvolution algorithm is commonly applied to restore the final high-resolution image. This approach is implemented in [5–7].

Besides ESF analysis, experiments with various image deconvolution methods conclude that the Richardson-Lucy algorithm yields the most favorable outcome [8, 9]. Another approach, a combination of Particle Swarm Optimization (PSO) and Bacterial Foraging Optimization (BFO) in blind deconvolution for neutron image deblurring, was proposed by the author in the study work [10]. However, this study depends on many varying parameters, such as the swarm size, inertia weight, and learning rates. Therefore, this study is not robust; the choices or parameters are sensitive and can lead to poor restoration performance. Recently, deep learning studies have been proposed to restore neutron images [11, 12]. However, due to the lack of training sets that contain clear neutron images and real degraded neutron images, the study in [11] uses X-ray images instead of neutron images as data drivers for the network.

All the studies mentioned earlier agreed that the quality of neutron images can be improved by the application of image deblurring. However, most of the studies required experimental work to estimate the PSF and used well-known non-blind deconvolution to restore neutron images. Hence, this study investigates the potential of the recent trend of blind deconvolution algorithms with regularization and optimization for neutron image deblurring. To the best of our knowledge, optimization-based blind deconvolution for neutron image applications has not yet received enough attention in the neutron community. The proposed method applies the estimation approach using a mathematical model to directly allow for the estimated PSF from a single blurred image without requiring experimental work and additional devices.

II. The Blind Deconvolution

In general, regularization is usually introduced into the optimization problem to avoid overfitting and reduce complexity. Over the last few years, blind deconvolution has experienced a renaissance. There have been numerous advanced blind deconvolution strategies using the maximum a posteriori (MAP) estimation framework for seeking both L and k. From Eq. (1), it is almost impossible to find an ultimate solution to restore L from B without prior knowledge k. In order to make the MAP-estimation framework well-posed, it requires additional constraints and prior knowledge of PSFs and sharp images. In general, the standard MAP-estimation framework contains a deconvolution cost function formed by the data fidelity term and the regularization term, which can be expressed as:

$$\min_{L,k} \|L * k - B\|_2^2 + \mu P(L) + \gamma P(k) \tag{2}$$

where $P(L)$ is a prior-related term for L and $P(k)$ is a prior-related term related to k. These two terms are regularization terms. μ and γ are the positive penalty parameters to balance the weight relationship between the fidelity term and the regularization term. Both $P(L)$ and

$P(k)$ are used to exploit the edge structures in the latent image and PSF, respectively.

The data fidelity term $\min_{L,k}\|L * k - B\|_2^2$ in (2) is a conventional constraint, which measures the likelihood between the recovered image and the blurred image. This term considers the noise distribution given in the blurred image. In most cases, the blurred images are degraded by Gaussian noise and a least-square data fidelity term is used to cope with Gaussian noise. Therefore, usually for this data fidelity term, L_2 norm is used to promote smoothness.

In the MAP-estimation framework for blind deconvolution, regularization constraints are typically used to enforce some prior knowledge or assumptions about the solution to the deconvolution problem. Regularization constraints can help to ensure that the solution is well-posed and stable, even in the presence of noise or other sources of uncertainty.

Previous blind deconvolution methods applied joint optimization problems and introduced sophisticated priors [13–15]. Therefore, these state-of-the-art methods are computationally demanding and time consuming. To address the computationally intensive issue in blind deconvolution, the utilization of regularization has proven to be an effective solution. Most recent regularization methods use the L_0 regularizer of ∇L (the gradient of L), and the L_2 norm is applied to constrain the PSF prior. Therefore, the objective function (2) can be written as follows:

$$\min_{L,k}\|L * k - B\|_2^2 + \mu\|\nabla L\|_0 + \gamma\|k\|_2^2 \tag{3}$$

where $\|\nabla L\|_0 = \{|\partial_x L| + |\partial_y L| > 0\}$.

One of the advantages of using $\|\nabla L\|_0$ is that the L_0 regularization gradient acts as edge preserving, which can quickly extract the main edge structure while eliminating isolated and harmful subtle details. Hence, this L_0 regularization can preserve the sparsity of image gradients. Meanwhile, L_2 is applied to constrain the PSF to encourage the smoothness of the nonzero elements in k.

III. Methodology

A. Proposed Image Prior

Using the standard blind deconvolution MAP-estimation model in (2), a new image prior $P(L)$ is proposed. The aim is to enforce sparsity of image prior, which helps accelerate the recovery of the intermediate latent image L during the iteration process of PSF estimation.

Conventional regularization-based blind deconvolution methods are complex and time-consuming. One promising approach to regularization methods is to incorporate the sparsity and non-overlapping patches strategy within the MAP estimation framework. The sparsity constraint promotes a solution where most elements are zero or close to zero, aiding in simplifying the representation. By inducing sparsity, the regularization term facilitates the recovery of intermediate latent images by reducing the impact of noise and irrelevant information while preserving the essential features. Concurrently, the non-overlapping patches approach can improve accuracy by focusing more on local details in a patch. Consequently, this non-overlapping approach also helps to converge faster. By using a combination of sparsity and non-overlapping patches, the scanning time can be reduced and the execution efficiency can be improved.

Recently, sparse image priors have made significant achievements in image deblurring [16–18]. A simple sparse prior based on a collection of local minimal pixels in non-overlapping patches has been proposed [19]. Referred to as patch-wise minimal pixels (PMP), this prior computes the low intensity of dark pixels in the non-overlapping patch. Inspired by the work in [19], the proposed approach drew inspiration from the inherent characteristic that non-overlapping patches tend to experience a reduction in high intensity values following the blurring process. In this study, we propose an improved PMP that exploits high-intensity pixels instead of low-intensity pixels as a mean for estimating the PSF iteratively for neutron images.

The proposed image prior is known as the enhanced patch-wise intensity (EPI) image prior. The EPI prior is a collection of local high-intensity (maximal) pixels in non-overlapping patches. The non-overlapping approach has been adopted in blind deconvolution to replace the conventional overlapping patch. Let a single channel grayscale neutron image L of size $m\times n$ represented as $L\in \mathbb{R}^{m\times n}$ be partitioned into d non-overlapping patches; with a patch size of $r\times r$. Here, adaptive patch size r is implemented, which is dependent on the image size. In this work, given the image size $m\times n$, the adaptive patch size r can be varied by the ratio formula, $r = \mathrm{SF}\times(\frac{m+n}{2})$, where SF is a scaling factor. SF can be a selection of 0.02, 0.025, 0.03, and 0.035. Hence, the number of patches will be $d = \left\lceil\frac{m}{r}\right\rceil \cdot \left\lceil\frac{n}{r}\right\rceil$, and $\lceil\cdot\rceil$ denotes the ceil operator. The EPI prior of image L is defined as:

$$\mathrm{EPI}(L)(i) = \max_{(x,y)\in\Omega_i} L(x,y) \tag{4}$$

where Ω_i denotes the pixel index location of the ith patch, i=1, 2, …, d, (x, y) denotes the pixel coordinates, and $\mathrm{EPI}(L)(i)$ denotes the collection of local maximal pixels over non-overlapping patches of L with patch-size $r\times r$.

It is easy to see that $\mathrm{EPI}(L)\in\mathbb{R}^d$ contains patch-wise (local) maximal pixels of L.

Introducing the EPI, the objective function (3) can be rewritten as:

$$\min_{L,k}\|L * k - B\|_2^2 + \mu\|\nabla L\|_0 + \alpha\|\mathrm{EPI}(L)\|_0 + \gamma\|k\|_2^2 \tag{5}$$

where α, μ, γ are positive weight parameters.

The first term is a fidelity term that constrains the convolution of the latent image L and the PSF k to be consistent with the blurred image. The second term is the L_0 regularization term of the image gradient, which can effectively smooth details and retain significant edge structures to facilitate PSF estimation. The third term uses the L_0 norm penalty to achieve sparsity induction on the

EPI of the latent image. For the last term, the L_2 norm is applied to constrain the kernel and obtain a stable solution.

Because it is difficult to solve (5) directly, the next step is applying the alternating optimization rule to (5), which splits the cost function into two sub-problems. The first sub-problem characterizes L using the following cost function:

$$L = \min_{L} \|L * k - B\|_2^2 + \mu \|\nabla L\|_0 \alpha \|\text{EPI}(L)\| \quad (6)$$

and for sub-problem k

$$k = \min_{k} \|L * k - B\|_2^2 + \gamma \|k\|_2^2 \quad (7)$$

B. Optimization Procedure

The optimization procedures for solving the proposed model are described briefly in this section. For the sake of simplicity, only important mathematical formulas are included in the discussion. Interested readers who wish to learn more about the optimization associated with the proposed method can read the relevant papers listed in the reference section.

In solving (6), a constraint is imposed to induce sparsity on EPI(L), indirectly speeding up the minimization process. Mathematically,

$$L = \min_{L} \|L * k - B\|_2^2 + \mu \|\nabla L\|_0 \quad (8)$$

subject to EPI(L)(i) $\sim p(x)$, for $i \in \{1, 2, \ldots, d\}$. As introduced in [19], the $p(x)$ is a probability density function of a hyper Laplacian distribution for x below a threshold such as 0.9. When comparing the sparsity of the clear image and its blurred counterpart, the expectation is that the clear image should be sparser. This is because blurring process tends to decrease the sparsity of an image due to the values of the high-frequency components are reducing. Hence, the EPI(L)(i) of clear images is much sparser than those of blurred images. This inequality property can be easily proven referring to [19, 20].

Then, with the half-quadratics strategy, we introduce the auxiliary variable G with respect to the image gradient ∇L, hence, (8) can be reformulated as follows:

$$\min_{L,G} \|L * k - B - B\|_2^2 + \beta \|\nabla L - G\|_2^2 + \mu \|G\|_0 \quad (9)$$

subject to EPI(L)(i)$\sim p(x)$, for $i \in \{1, 2, \ldots, d\}$.

The closed-form solution of (9) can be obtained using the FFT algorithm. Mathematically:

$$L = \mathcal{F}^{-1}\left(\frac{\overline{\mathcal{F}(k)}\mathcal{F}(B) + \beta\left(\overline{\mathcal{F}(\nabla_h)}\mathcal{F}(G_h) + \overline{\mathcal{F}(\nabla_v)}\mathcal{F}(G_v)\right)}{\overline{\mathcal{F}(k)}\mathcal{F}(k) + \beta\left(\overline{\mathcal{F}(\nabla_h)}\mathcal{F}(\nabla_h) + \overline{\mathcal{F}(\nabla_v)}\mathcal{F}(\nabla_v)\right)}\right) \quad (10)$$

where $\mathcal{F}(.)$ and $\mathcal{F}^{-1}(.)$ represent the FFT and inverse FFT respectively. $\overline{\mathcal{F}(\cdot)}$ is the complex conjugate operator. ∇_v, ∇_h denote vertical and horizontal differential operators, respectively.

The sub-problem k in (7) is based on image intensity. To obtain a more accurate solution, it is commonly estimated in the gradient space rather than performing the estimation in the intensity space, which is more conducive to an accurate estimation of PSF.

$$k = \min_{k} \|\nabla L * k - \nabla B\|_2^2 + \gamma \|k\|_2^2 \quad (11)$$

The closed-form solution to (11) can be calculated by FFT,

$$k = \mathcal{F}^{-1}\left(\frac{\overline{\mathcal{F}(\nabla_h L)}\mathcal{F}(\nabla_h B) + \overline{\mathcal{F}(\nabla_v L)}\mathcal{F}(\nabla_v B)}{\overline{\mathcal{F}(\nabla_h L)}\mathcal{F}(\nabla_h L) + \overline{\mathcal{F}(\nabla_v L^i)}\mathcal{F}(\nabla_v L) + \gamma}\right) \quad (12)$$

Algorithm 1. Proposed PSF Estimation with EPI prior algorithm

Input: Blurred image B

Initialize the intermediate image L and PSF k;

For $i = 1 : iter$ **do**

Estimate L according to (10)

Estimate k according to (12)

End For

Output: estimated PSF k, intermediate latent image L

In this study, the algorithm is implemented in MATLAB.

C. Multi-Layer Pyramid Iterative Alternating Approach

The restoration process consists of two main steps: PSF estimation and final non-blind deconvolution. The overall workflow is shown in Fig. 2. The proposed PSF estimation is executed in a coarse-to-fine manner, which is commonly used in established methods [20–23]. In this scheme, the input blurred image is down-scaled to create a series of reduce-resolution image L, while the PSF k is upscaled. The results of the coarse layer are up-sampled with the bilinear interpolation method as the initialization of the next fine layer.

Inside each layer, the alternate minimization process iterates between: i) latent image estimation using (10), ii) kernel estimation using (12). At each pyramid layer, (10) and (12) are refined through the number of iterations iter = 5.

We first initialize the intermediate image L and PSF k according to the blurry input. The Gaussian PSF, with a size of 7×7 is fixed at the first iteration in the coarsest layer. At the start of minimization, the weight μ is set to a high value to ensure the restoration of strong edges and the removal of details. In a limited iteration process, L is computed with the EPI prior. The EPI prior in each non-overlapping patch is obtained according to the definition of EPI prior in (4).

Next, k is obtained from the estimated intermediate latent image L and a given blurred image. Then the estimated k is up-scaled and used as the initial point of the next layer estimation. After solving (12), the negative values of k are set to zero and normalized so that their values sum to one. After that, k is centered and renormalized.

The main purpose of the iterative alternating optimization in the multi-layer approach is to avoid falling into the local minimum and progressively refine the PSF k, while the estimated intermediate latent image L during the iteration has no direct effect on the deblurring output.

Once the final estimated k is achieved, the final restoration is employed using the final estimated k and B as the inputs, as shown by the green arrow in Fig. 2. This work adopts the non-blind deconvolution algorithm [23] to reduce the ring artifact.

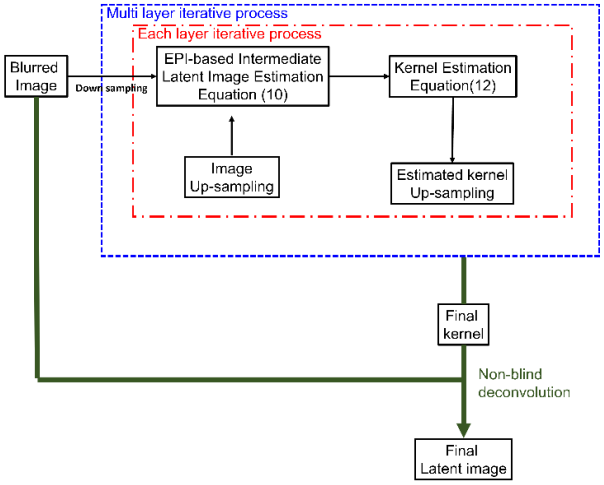

Fig. 2. Overall framework of the multi-layer iterative alternating scheme of the EPI-based method.

D. Neutron Radiography Facility at RTP

All neutron images presented in this work were acquired at the Malaysia Nuclear Agency, which houses the Research TRIGA PUSPATI (RTP) reactor. The RTP is a swimming pool-type light water research reactor with enriched uranium-zirconium-hydride fuel and graphite reflector. The nominal power of the RTP is 1 MW, and it is considered a low-power research reactor. The RTP is a pool-type light water research reactor with a nominal power of 1.0 MW, which falls under the low-flux research reactor category. The maximum flux at the core is 10^{13} n/cm²/s. The RTP has three radial beam ports, one tangential beam port, and one thermal column. The radial piercing beam ports, which directly point at the core, have higher flux and larger gamma and epithermal neutron backgrounds. On the other hand, the tangential beam port has a lower neutron flux and reduced gamma contamination.

The neutron radiography facility at the RTP was constructed at one of the radial beam ports. The main components of the neutron facility at the RTP are illustrated in Fig. 3. Referring to Fig. 3(b), the neutron radiography facility at RTP consists of a 232-meter-long divergent collimator with a 3-cm-diameter aperture [24, 25]. This divergent collimator is used to channel the neutron beam from the reactor core to the sample and ultimately to the scintillator, where neutrons are converted into visible light radiation. The light is then focused onto the CCD camera through a tilted mirror to avoid a direct radiation beam. To perform neutron radiography, the sample is positioned at a distance of 80 cm from the beam port exit. Since the neutron entrance aperture diameter is 3 cm and the distance between the inlet aperture and the image plane is 312 cm, this gives a L/D ratio of approximately 104. This low L/D ratio is the main reason for the degradation of neutron images, as previously explained.

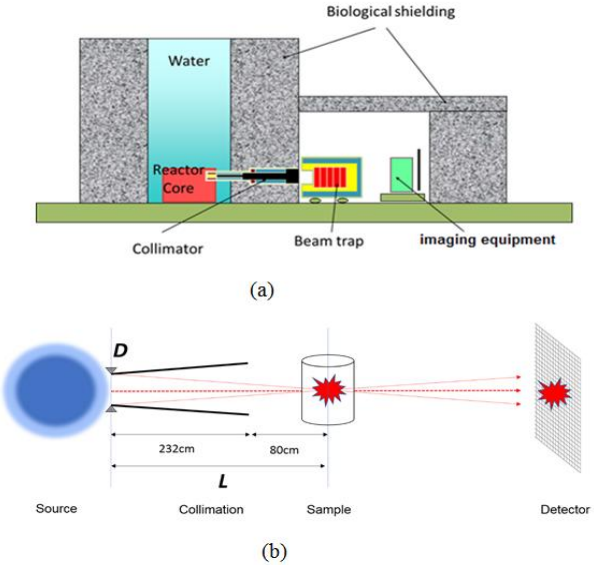

Fig. 3. Schematic picture of neutron radiography facility at RTP (a) cross-section view (b) The collimation set-up showing the distance between aperture and sample L, and the aperture size of inlet collimator D.

TABLE I: MAIN PARAMETERS OF THE NEUTRON FACILITY AT RTP

Parameters	Specification
Beam line	Radial
Neutron spectrum	Thermal
Flux at sample position	10^4 n/cm²/s
Length collimator [cm]	232
Distance outer collimator to sample[cm]	80
L/D	104

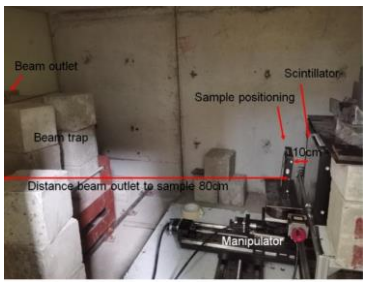

Fig. 4. A photo of neutron radiography facility at RTP.

Fig. 4 shows the experimental setup at the neutron radiography facility at RTP. All parameters of the neutron facility in RTP are shown in Table I.

Another source of degradation is impulse noise due to the generation of high-energy gamma radiation at the radial beam port, as discussed earlier. The radial beam port contains high-energy gamma radiation compared to the tangential beam port. At 750 kW of nominal operating power, the flux intensity at the sample position is 10^4 n/cm²/s, which is low compared to state-of-the-art facilities. A typical flux of reactor-based neutron radiography facilities at the sample position is 10^7 n/cm²/s. Meanwhile, a typical flux of spallation-based neutron radiography facilities at the sample position is 10^9 n/cm²/s. Low thermal flux means neutron radiographic images produced by RTP exhibit a low dynamic range. One way to overcome this problem is to increase the exposure time, which in turn

enhances the noise. As a trade-off between dynamic range and noise, all images shown in this paper were acquired with a 200-second exposure time.

The imaging detector is a scintillator-based CCD type using a 16-bit cooled CCD camera. The neutron beam strikes a 0.1-mm-thick green scintillation screen. The lights produced by the scintillation screen were recorded on the CCD, which comprises 2200 × 2750 pixels. A double-surface coating was used to keep the camera away from the direct neutron beam. Additional shielding was used to protect the electronic parts from the direct neutron beam. There are limitations in the imaging system. This type of standard CCD-based detector suffers from blurring from the lens system due to the large distance between the scintillator and the lens system.

All acquired neutron images were processed using Remove Outlies function in open-source ImageJ software to remove the significant noise. This noise mainly added during acquisition. Then, the low dynamic range image contrast is adjusted to widen the dynamic range. The neutron image was too large, causing the algorithm to run very slowly; therefore, the original image is cropped for the selected area. Then, the denoised blurred image is normalized between 1 and 0 from the original 16-bit digital values.

IV. Results and Discussion

In the following, we present some experiment deblurring results using the proposed method and compared with the conventional edge-based neutron image deblurring method. Fig. 5 shows a small water-pump, Fig. 6 shows an electronic board, and Fig. 7 shows electronic digital camera. The aim is to estimate PSF and the estimated PSF is then input into a non-blind deconvolution method. As discussed in previous section, within the neutron community, the ESF and LSF based methods is the easiest approach used for PSF estimation and iterative RL deconvolution is commonly used for final restoration. In this study, 15 iterations were used for final deblurring.

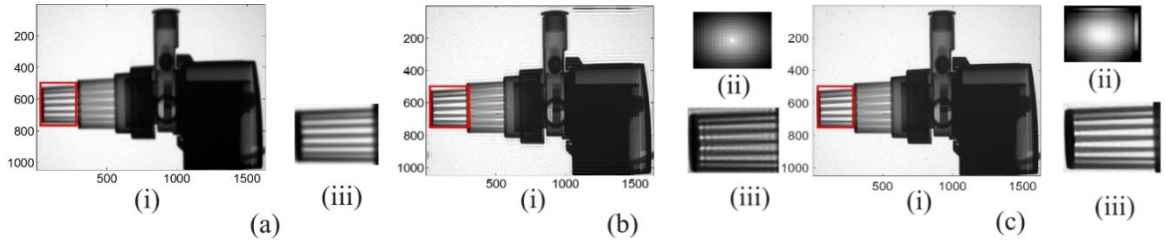

Fig. 5. Iterative image deblurring comparing conventional and proposed methods. (i) neutron image, (ii) the estimated PSF and (iii) selected regions are zoomed-in to highlight small and fine details in red box, (a) blurred image, (b) and (c) are restored image by the conventional and proposed methods respectively.

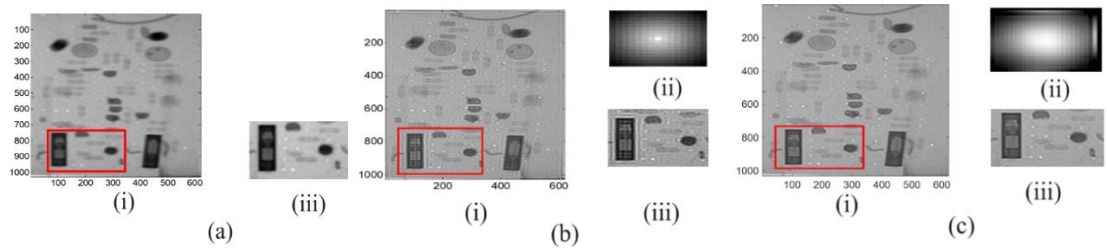

Fig. 6. Restoration comparing conventional and proposed methods. (i) neutron image, (ii) the estimated PSF and (iii) selected regions are zoomed-in to highlight small and fine details in red box, (a) blurred image, (b) and (c) are restored image by the conventional and proposed methods respectively.

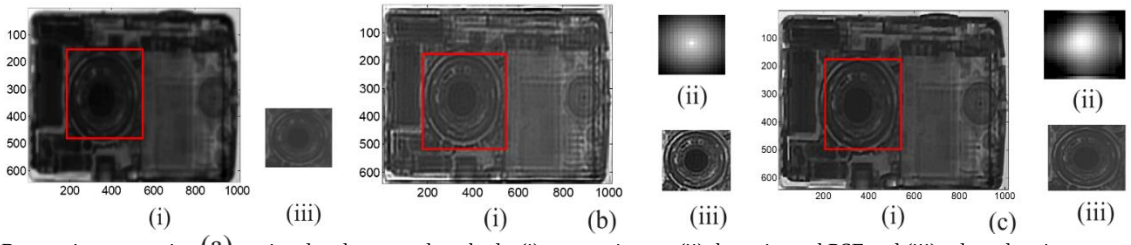

Fig. 7. Restoration comparing (a) ventional and proposed methods. (i) neutron image, (ii) the estimated PSF and (iii) selected regions are zoomed-in to highlight small and fine details in red box, (a) blurred image, (b) and (c) are restored image by the conventional and proposed methods respectively.

The neutron images involved no ground-truth images. Besides visual inspection, to evaluate the deblurring performance of the neutron images, the BRISQUE index is used to assess the quality of the neutron images.

As seen clearly from Fig. 5 (i) to Fig. 7 (i), the proposed method performed exceptionally well compared with conventional methods. Visually, the structure of the deblurred images in the proposed method appears relatively sharper and clearer compared with the conventional method. It can be seen that the conventional method using iterative Richardson-Lucy algorithm produces slightly ringed artifacts at the top and bottom. Even though the appearance of structures in Fig. 5 (iii) to Fig. 7 (iii) has improved slightly, they are still blurry. This

is due to the final deblurring results, which depend on the accuracy of the estimated PSF. From Fig. 5 (ii) to Fig. 7 (ii), the multi-layer iterative alternating approach in the proposed method produced a refined *k*, while the ESF approach in the conventional method produced an asymmetric *k*.

Referring to Table II, the proposed model has better performance in terms of BRISQUE measures. On average, the proposed method resulted in a BRISQUE index of 45.88 compared to the conventional method's 57.35 and blur's 49.21.

TABLE II: THE DEBLURRING PERFORMANCE COMPARING THE CONVENTIONAL AND PROPOSED METHODS IN TERMS OF BRISQUE QUALITY INDEX

Unit	Conventional edge method	Proposed method	Blur
Water-pump	57.03	48.45	49.63
Board	56.80	43.51	48.50
Camera	58.23	45.68	49.50
Average	**57.35**	**45.88**	**49.21**

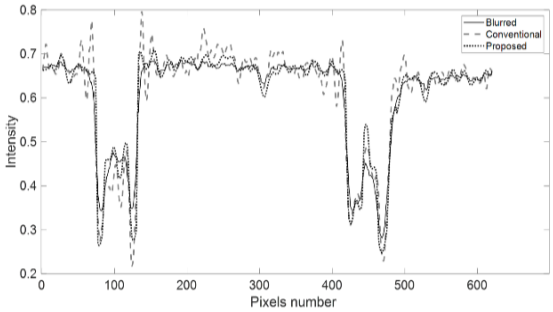

Fig. 8. Line profile of Fig. 6 (a) to (c) (i) through the horizontal line y-800. Analyzing this profile allows us to assess the impact of the proposed technique on the image features in the region of interest.

To demonstrate the effectiveness of the proposed technique, Fig. 8 shows a line profile which is obtained by sampling the pixel intensities along the horizontal line positioned at $y = 800$.

Please note that it is not a fair comparison to compare CPU times in both methods due to the different approaches; the conventional method applied a non-iterative PSF estimation process, while the proposed method utilized an iterative PSF estimation process. The point to be made here is that the blind deconvolution method can be used to estimate PSF compared to normal practice, which often relies on a trial-and-error approach.

V. CONCLUSION

This paper describes a robust method for deblurring a single blurred neutron image. An improved image prior for image deblurring in a blind deconvolution framework is presented. A coarse-to-fine multi-layer iterative approach is also implemented within the MAP framework. Overall, these steps resulted in a more accurate estimation of PSF and, hence, superior restoration performance for neutron images.

CONFLICT OF INTEREST

The authors declare no conflict of interest.

AUTHOR CONTRIBUTIONS

Y. Khairiah is the primary researcher of the work and the main author of the paper. A. Mohd Zaid and I. Haidi have contributed expertise in image processing. They have acted in supervisory role. All authors had approved the final version.

REFERENCES

[1] N. Kardjilov, I. Manke, R. Woracek *et al*, "Advances in neutron imaging," *Materials Today*, vol. 21, no. 6. 2018. doi: 10.1016/j.mattod.2018.03.001.

[2] E. H. Lehmann and D. Mannes, "Neutron radiography and tomography," *Encycl. Archaeol. Sci.*, pp. 1–6, 2018, doi: 10.1002/9781119188230.saseas0407.

[3] A. Tengattini, N. Lenoir, E. Andò *et al*, "Neutron imaging for geomechanics: A review," *Geomech. Energy Environ.*, 2020, doi: 10.1016/j.gete.2020.100206.

[4] E. Lehmann, P. Trtik, and D. Ridikas, "Status and perspectives of neutron imaging facilities," *Phys. Procedia*, vol. 88, pp. 140–147, 2017, doi: 10.1016/j.phpro.2017.06.019.

[5] B. Masschaele, M. Dierick, L. Van Hoorebeke *et al*, "Neutron CT enhancement by iterative de-blurring of neutron transmission images," *Nucl. Instruments Methods Phys. Res.*, vol. 542, pp. 361–366, 2005, doi: 10.1016/j.nima.2005.01.162.

[6] K. Yazid, M. Z. Abdullah, M. R. Mohamed Zin *et al*, "Performance of imaging system at Reactor TRIGA Mark II PUSPATI," *IOP Conf. Ser. Mater. Sci. Eng.*, vol. 785, #012023, 2020, doi: 10.1088/1757-899x/785/1/012023.

[7] K. Yazid and M. Z. Abdullah, "Point spread function estimation for neutron images," in *Proc. of the 2019 2nd Int. Conf. on Electronics and Electrical Engineering Technology*, 2019, pp. 87–91.

[8] F. Grunauer, "Design, optimization, and implementation of the new neutron radiography facility at FRM-II," 2005, [Online]. Available: https://mediatum.ub.tum.de/doc/603112/document.pdf

[9] W. Jin, "Image restoration in neutron radiography using complex-wavelet denoising and Lucy-richardson deconvolution," in *Proc. of 2006 8th Int. Conf. Signal Processing*, 2006, doi: 10.1109/ICOSP.2006.345571.

[10] S. Saadi, M. Bettayeb, and A. Guessoum, "Deconvolution of neutron degraded images: Comparative study between TSVD, Tikhonov regularization and particle swarm optimization algorithm," *Eng. Lett.*, vol. 18, no. 3, 2010. www.engineeringletters.com. Retrieved 2 Dec 2021

[11] J. Yang, C. Zhao, S. Qiao *et al*, "Deep learning methods for neutron image restoration," *Ann. Nucl. Energy*, vol. 188, #109820, Aug. 2023, doi: 10.1016/j.anucene.2023.109820.

[12] C. Scatigno and G. Festa, "Neutron imaging and learning algorithms: new perspectives in cultural heritage applications," *J. Imaging*, vol. 8, no. 10, 2022, doi: 10.3390/jimaging8100284.

[13] R. Fergus, B. Singh, A. Hertzmann, "Removing camera shake from a single photograph," *ACM SIGGRAPH 2006 Papers*, pp. 787-794. doi: 10.1145/1179352.1141956

[14] Q. Shan, J. Jia, and A. Agarwala, "High-quality motion deblurring from a single image," *ACM Trans. Graph.*, vol. 27, no. 3, 2008, doi: 10.1145/1360612.1360672.

[15] D. Krishnan, T. Tay, and R. Fergus, "Blind deconvolution using a normalized sparsity measure," in *Proc. IEEE Comput. Soc. Conf. Comput. Vis. Pattern Recognit.*, 2011, pp. 233–240.

[16] Z. Xu, H. Chen, and Z. Li, "Fast blind deconvolution using a deeper sparse patch-wise maximum gradient prior," *Signal Process. Image Commun.*, vol. 90, 2021, doi: 10.1016/j.image.2020.116050

[17] D. Yang, X. Wu, and H. Yin, "Blind image deblurring via a novel sparse channel prior," *Mathematics*, vol. 10, no. 8, pp. 1–18, 2022, doi: 10.3390/math10081238

[18] Z. Xu, H. Chen, and Z. Li, "Blind image deblurring using group sparse representation," *Digit. Signal Process. A Rev. J.*, vol. 102, #102736, 2020, doi: 10.1016/j.dsp.2020.102736.

[19] F. Wen, R. Ying, Y. Liu, *et al* , "A simple local minimal intensity prior and an improved algorithm for blind image deblurring," *IEEE Trans. Circuits Syst. Video Technol.*, 2020, doi: 10.1109/TCSVT.2020.3034137.

[20] J. Pan, D. Sun, H. Pfister, and M. H. Yang, "Deblurring images via

dark channel prior," *IEEE Trans. Pattern Anal. Mach. Intell.*, vol. 40, no. 10, pp. 2315–2328, 2018.
[21] J. Pan, R. Liu, Z. Su, and X. Gu, "Kernel estimation from salient structure for robust motion deblurring," *Signal Process. Image Commun.*, vol. 28, no. 9, pp. 1156–1170, 2013.
[22] Y. Yan, W. Ren, Y. Guo, R. Wang, and X. Cao, "Image deblurring via extreme channels prior," in *Proc. of 30th IEEE Conf. Comput. Vis. Pattern Recognition*, 2017, pp. 6978–6986.
[23] J. Pan, Z. Hu, Z. Su, and M. Yang, "L_0 -regularized intensity and gradient prior for text images deblurring and beyond supplemental material," in *Proc. of 2014 IEEE Conf. on Comput. Vis. Pattern Recognit.*, 2014, pp. 2901–2908.
[24] M. S. Sarkawi, J. Zainal, and R. Jamro, "Beam characterization of new neutron radiography facility at TRIGA Mark II PUSPATI research reactor Beam characterization of new neutron radiography facility at TRIGA Mark II PUSPATI research reactor," *IOP Conference Series Materials Science and Engineering*, 2019. doi: 10.1088/1757-899X/555/1/012018
[25] M. R. M. Zin, R. Jamro, A. Azman *et al* "The development of neutron imaging instrument at PUSPATI TRIGA MARK II nuclear research reactor," *Journal of Radiation and Nuclear Application*, vol. 5, no. 2, pp. 81–86, 2020.

Yazid Khairiah earned her Master's degree from Universiti Sains Malaysia in 2011, showcasing her commitment to academic excellence and passion for technological advancements. She is currently work as researcher at Malaysian Nuclear Agency. Currently, she serves as a researcher at the Malaysian Nuclear Agency, where she actively contributes to cutting-edge research initiatives. Her work revolves around the fascinating realms of neutron and X-ray imaging, computed tomography, and the innovative intersections of deep learning, artificial intelligence, and machine learning.

Abdullah Mohd Zaid and the other authors may include biographies and photographs at the end of regular papers. Mohd Zaid graduated from Universiti Sains Malaysia (USM) with a B. App. Sc. degree in Electronic in 1986 before joining Hitachi Semiconductor (Malaysia) as a Test Engineer. In 1989, he commenced an M.Sc. in Instrument Design and Application at University of Manchester Institute of Science and Technology, UK. He remained in Manchester, carrying out research in Electrical Impedance Tomography at the same university, and received his Ph.D. degree in 1993. In the same year he joined USM as a lecturer and remained with this university until his official retirement in November 2022. His principle research area is in Instrumentation and Sensing which covers topics such ultra-wide band imaging, computer vision applications and microwave tomography. He has published more than 140 research articles in international journals as IEEE, IET, IOP, etc. One of his papers was awarded The Senior Moulton medal for the best article published by the Institute of Chemical Engineering in 2002. He is a Fellow of Institutions of Engineering and Technology, Chartered Electrical Engineer, Chartered Engineer, and editorial board member of the Measurement Science and Technology since 2017. He has served as the dean of the School of Electrical and Electronic Engineering, 2006-2015, and the director of Collaborative Microelectronic Design Excellence Centre (CEDEC), 2016-2018. Presently he is an Honorary Professor at USM's School of Electrical and Electronic Engineering.

Ibrahim Haidi received his B.Eng degree in electrical and electronic engineering from Universiti Sains Malaysia, Malaysia. He received his Ph.D degree in image processing from University of Surrey, United Kingdom in 2005. His research interests include digital image and signal processing, and analysis.